Int J Fract (2016) 200:99–113
DOI 10.1007/s10704-016-0123-9

IUTAM PARIS 2015

Dynamic stability of biaxially strained thin sheets under high strain-rates: response to local perturbations

G. Wen · N. Triantafyllidis

Received: 25 September 2015 / Accepted: 26 May 2016 / Published online: 16 June 2016

Abstract This work pertains to the stability of structures under rapid loading rates when inertia is taken into account. In contrast to the widely used approach in the relevant literature, which is based on the method of modal analysis to determine the structure's fastest growing eigenmode—meaningful only for cases where the velocity of the perfect structure is significantly lower than the associated characteristic wave propagation speeds—the present study analyzes the time-dependent response to spatially localized perturbations of the transient (time-dependent) states of these structures, in order to understand the initiation of the corresponding failure mechanisms. We are motivated by the experimental studies of Zhang and Ravi-Chandar (Int J Fract 142:183-217, 2006), Int J Fract 163:41-65, (2010) on the high strain-rate expansion of thin rings and tubes, which show no evidence of a dominant wavelength in their failure mode and no influence of strain-rate sensitivity on the necking strains. Recently, Ravi-Chandar and Triantafyllidis (Int J Solids Struct 58:301-308, 2014) studied the dynamic stability of an incompressible, nonlinearly elastic bar at different strain-rates by following the evolution of localized small perturbations introduced at different times. The same approach is followed here for the biaxial stretching of thin plates, where we follow the time evolution of spatially localized perturbations and their interactions. The nonlinear time evolution of a such a perturbation is studied numerically and it is shown that these structures are stable until the time when the condition for the loss of ellipticity is reached. An analytical method, based on linearization, is used to define the size of the influence zone of a point-wise perturbation and we study its dependence on constitutive laws and loading conditions.

Keywords Inertia · Energy methods · Nonlinear elasticity

G. Wen · N. Triantafyllidis (✉)
Laboratoire de Mécanique des Solides, C.N.R.S.
UMR7649 École Polytechnique, 91128 Palaiseau, France
e-mail: nick@lms.polytechnique.fr

N. Triantafyllidis
Département de Mécanique, École Polytechnique,
91128 Palaiseau, France

N. Triantafyllidis
Aerospace Engineering Department and Mechanical Engineering Department (emeritus), The University of Michigan, Ann Arbor, MI 48109-2140, USA

Contents

1 Introduction

The issue of dynamic stability of structures is an important engineering problem and as such has drawn considerable attention. The first investigation in this area appears to be the work of Koning and Taub (1933), who investigated the influence of inertia in a simply supported imperfect column subjected to a sudden axial load. A substantial amount of work followed that investigated the response of, mainly elastic, structures to impulse or time-dependent loads. As a result, and due to the many possible definitions for the stability of time-dependent systems, the term *dynamic stability* encompasses many classes of problems and different physical phenomena and has many interpretations, with inertia being the only common denominator.

In the absence of inertia, the processes of failure by a bifurcation instability mode in elastic solids and structures are well understood (e.g. Brush and Almroth (1975)) and a general asymptotic analysis, termed Lyapunov-Schmidt-Koiter (LSK), has been developed for their study. The first effort to use the LSK general analysis for the dynamic stability problem of an elastic structure appears to be Budiansky and Hutchinson (1964), where the authors proposed an asymptotic analysis of the time-dependent problem using the eigenmodes of the static problem.

Another idea, popular in fluid mechanics, has also been adopted for the dynamic stability analysis of solids with more general constitutive laws under high rates of loading, according to which one seeks the solid's fastest growing eigenmode, or the wavelength associated with lowest necking strain. This method has been repeatedly applied in the study of the dynamic stability of various elastoplastic structures (bars, rings, plates, shells e.t.c.) under high loading rates where the failure pattern and size of fragments is of interest (e.g. see Shenoy and Freund (1999), Sorensen and Freund (2000), Guduru and Freund (2002), Mercier and Molinari (2003), Zhou et al. (2006), Xue et al. (2008), Mercier et al. (2010), Jouve (2015)).

However, recent experimental evidence from rapidly expanding electromagnetically loaded metallic rings by Zhang and Ravi-Chandar (2006, 2008) finds no evidence of a dominant wavelength at the necked pattern of the rings. Moreover, they find no experimental evidence of influence of strain rate on the necking strains, which are consistent with maximum force criterion of a rate independent constitutive law (Considère criterion).

As explained by these authors, using the fastest growing eigenmode to predict the onset of failure is physically meaningful provided that some characteristic velocity of the principal solution—e.g. ring/tube expansion rate—is much slower than the speed of propagation of perturbations in the solid or structure at hand. For high loading rates, commensurate with some characteristic wave propagation speed in the structure, a novel approach to the stability analysis is required, namely the study of the evolution of localized perturbations.

We are motivated by the experimental studies of Zhang and Ravi-Chandar (2006, 2010) on the high strain-rate expansion of thin rings and tubes, which show no evidence of a dominant wavelength in their failure mode and no influence of strain-rate sensitivity on the necking strains—the onset of failure of an electromagnetically loaded, dynamically expanding tube is shown in Fig. 1, where one can observe a rather random failure mode. Recently, Ravi-Chandar and Triantafyllidis (2015) studied the dynamic stability of an incompressible, nonlinearly elastic bar at different strain-rates by following the evolution of localized small perturbations introduced at different times. The same approach is followed here for the biaxial stretching of thin plates, where we follow the time evolution of spatially local-

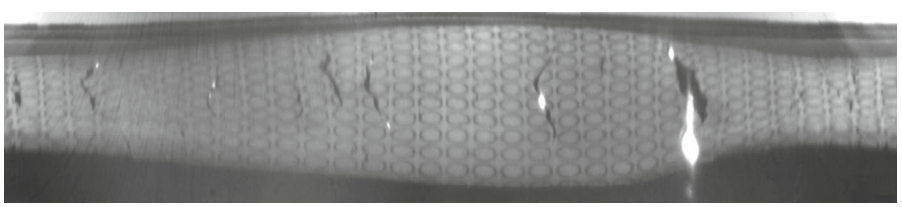

Fig. 1 Unfolded conical mirror image for an electromagnetically expanding Al 6061-O tube test (from Zhang and Ravi-Chandar (2010)), showing the *onset* and evolution of necks under high strain rate loading; notice the absence of a dominant wavelength in the failure pattern

ized perturbations and their interactions. Following this introduction, in Sect. 1, the formulation of the problem (definition of influence zones and algorithm for the nonlinear FEM calculations) is presented in Sect. 2. Results are given in Sect. 3, starting with the description of the constitutive models and following with the numerical study of the nonlinear time evolution of a such a perturbation showing that these structures are stable until the time when the condition for the loss of ellipticity is reached. In the same section we present an analytical method, based on linearization, to define the size of the influence zone of a point-wise perturbation and we study its dependence on constitutive laws and loading conditions. The presentation is concluded in Sect. 4.

2 Problem formulation

This section starts with the presentation of the model for the propagation of perturbation about a point defect on a biaxially strained, rate-independent, flat plate of infinite extent by studying the evolution of influence zones (linearized approach). The setting of the corresponding nonlinear problem, which is treated numerically, is presented subsequently.

2.1 The influence zones of a biaxially strained elastoplastic plate

We consider a 2D thin, flat plate (idealized as a membrane) of infinite extent and uniform initial thickness H subjected to a biaxial stretching as shown in Fig. 2. To avoid in-plane acceleration terms in the unperturbed solution of the perfect plate, the following stretch ratios are being imposed at infinity:

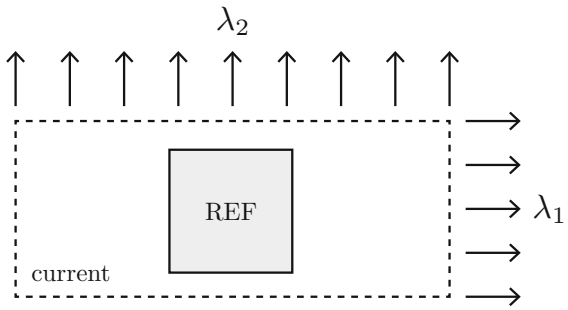

Fig. 2 A schematic diagram of a biaxially strained plate

$$\lambda_1 = 1 + (c\cos\psi)t\ , \quad \lambda_2 = 1 + (c\sin\psi)t\ . \tag{2.1}$$

Hence a uniaxial straining corresponds to $\tan\psi = 0$, balanced biaxial straining to $\tan\psi = 1$, while a uniaxial stressing is approximated by $\tan\psi = -1/2$ (assuming incompressibility and valid only initially for small strains. A more accurate value for finite strains depends on constitutive response).

In the absence of body forces the equations of motion of the thin plate can be put in the form[1]:

$$\frac{\partial N_{\alpha\beta}}{\partial X_\beta} = \rho_0 \frac{\partial^2 u_\alpha}{\partial t^2}\ , \tag{2.2}$$

where $N_{\alpha\beta}$ is the nominal (force/reference thickness) stress resultant, ρ_0 the reference mass density, X_α the reference geometric coordinates and $u_\alpha(\mathbf{X}, t)$ the corresponding displacement of a material point initially at $\mathbf{X}$ in the Lagrangian description. For simplicity the reference configuration is identified with the stress-free configuration of the plate.

The plate's constitutive equation is assumed to be rate-independent with the following relation between the time derivative of the stress measure $\dot{N}_{\alpha\beta}$ and rate of deformation gradient $\dot{F}_{\alpha\beta}$[2]:

$$\dot{N}_{\alpha\beta} = \mathcal{L}_{\alpha\beta\gamma\delta}\dot{F}_{\gamma\delta}\ ; \quad F_{\epsilon\zeta} = \delta_{\epsilon\zeta} + \frac{\partial u_\epsilon}{\partial X_\zeta}\ , \tag{2.3}$$

where $\mathcal{L}_{\alpha\beta\gamma\delta}$ are the plane stress incremental moduli of the plate, which in general depend on the current state of stress plus the deformation history represented by a set of internal variables. These moduli obtained from the 3D version of the constitutive equation $\dot{\Pi}_{ji} = L_{ijkl}\dot{F}_{kl}$ (relating the rate of the first Piola-Kirchhoff stress $\dot{\Pi}_{ji}$ to its work conjugate quantity $\dot{F}_{kl}$) plus the plane stress condition $\dot{\Pi}_{3i} = 0$ and the orthotropy of the plate with respect to the thickness direction. For the case of a hyperelastic material the stress measures are derivable from a potential i.e. $N_{\alpha\beta} = \partial W/\partial F_{\alpha\beta}$ in which case $\mathcal{L}_{\alpha\beta\gamma\delta} = \partial^2 W/\partial F_{\alpha\beta}\partial F_{\gamma\delta}$ where $W(\mathbf{F})$ is the 2D strain energy density of the plate.

Of interested here is the propagation of the localized perturbation about $\mathbf{X} = \mathbf{0}$. Using Δf to denote

[1] Here and subsequently Greek indexes range from 1 to 2 while Latin indexes range from 1 to 3.

[2] Here and subsequently, superimposed dot denotes time differentiation $\dot{f} \equiv \partial f(\mathbf{X}, t)/\partial t$.

the difference between the perturbed and unperturbed values respectively of a field quantity f and exploiting the fact that the principal solution is homogeneous (i.e. independent of $\mathbf{X}$), one obtains the following systems governing the evolution of perturbation[3]:

$$\mathcal{L}_{\alpha\beta\gamma\delta}\frac{\partial^2\Delta u_\gamma}{\partial X_\delta \partial X_\beta} = \rho_0 \frac{\partial^2 \Delta u_\alpha}{\partial t^2} \ . \tag{2.4}$$

We follow the propagation of the perturbation in all directions $\mathbf{n}$ and for this propose we consider solutions of the form:

$$\Delta u_\alpha(\mathbf{X}, t) = U_\alpha f\left(Vt - n_\alpha X_\alpha\right) \ , \tag{2.5}$$

where $f(z)$ is an arbitrary function of $z \in \mathbb{R}$, U_α is the perturbation amplitude and V its speed of propagation.

Introducing (2.5) into (2.4) one finds that $(V)^2$ is one of the two eigenvalues of $\mathcal{L}_{\alpha\beta\gamma\delta}n_\beta n_\delta \equiv A_{\alpha\gamma}(\mathbf{n})$ which is the acoustic tensor along $\mathbf{n}$:

$$\left[\mathcal{L}_{\alpha\beta\gamma\delta}n_\beta n_\delta - \rho_0 (V)^2 \delta_{\alpha\gamma}\right] U_\gamma = 0 \ . \tag{2.6}$$

The absence of any characteristic length ratio in the infinite flat plate, leads do the following non-dimensionalization of perturbation velocity (v), distance (χ), and time (τ) for this problem

$$v \equiv V\ [G/\rho_0]^{-1/2} \ ; \quad \chi \equiv Xc\,[G/\rho_0]^{-1/2} \quad \tau \equiv ct, \tag{2.7}$$

where $[G/\rho_0]^{-1/2}$ is the shear wave propagation speed at zero strain (G being the corresponding shear modulus of the plate at zero strain) and c the straining speed introduced in (2.1).

We are now in a position to estimate the extent of the zone influenced by a point-wise perturbation introduced at the onset of deformation ($\tau = 0$) in the plate until the onset of a necking localization, characterized by the loss of ellipticity in the perfect thin plate. We also call this perturbation an *initial defect*, since the introduction of the spatially localized perturbation at the beginning of the loading process is equivalent to a the presence of a defect in the plate. To this end we define the lowest and highest dimensionless wave propagation speeds v_- and v_+ which are the lowest and highest eigenvalues of the acoustic tensor according to (2.6) appropriately non-dimensionalized with the help of (2.7).

For a given time τ, on can thus define the influence zones χ_- and χ_+ determined by:

$$\begin{aligned}\chi_-(\phi, \tau) &\equiv \int_0^\tau v_-\left(\phi, \tau'\right) d\tau' \ , \\ \chi_+(\phi, \tau) &\equiv \int_0^\tau v_+\left(\phi, \tau'\right) d\tau' \ ,\end{aligned} \tag{2.8}$$

which are the distances traveled at time τ by the slow and fast wave fronts respectively along direction ϕ (recall $n_1 = \cos\phi, n_2 = \sin\phi$) (Fig. 3).

The perturbation can no longer propagate along a direction ϕ once its lowest speed reaches $v_- = 0$, which occurs at time $\tau_e(\phi)$ (subscript e standing for loss of ellipticity in the incremental equilibrium equations):

$$\begin{aligned}&v_-\left(\phi, \tau_e(\phi)\right) = 0 \\ &\quad \left(v_-(\phi, \tau) > 0 \text{ for } 0 \le \tau < \tau_e(\phi)\right) \ .\end{aligned} \tag{2.9}$$

The locus of points reached by the wave propagating along a given direction ϕ until $v_- = 0$ is given by:

$$\chi_e(\phi) \equiv \int_0^{\tau_e(\phi)} v_-\left(\phi, \tau'\right) d\tau' \ , \tag{2.10}$$

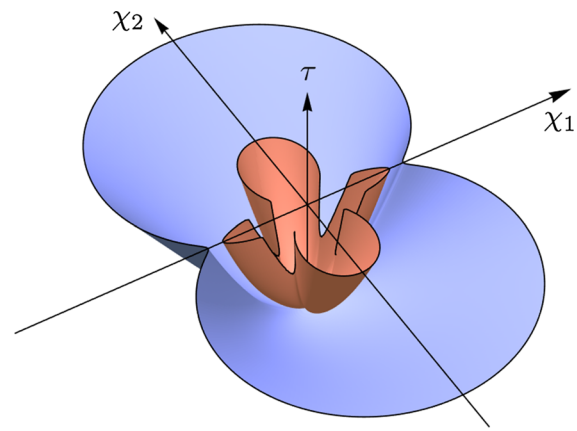

Fig. 3 Typical influence cone of an initial ($\tau = 0$) perturbation at $\mathbf{X} = 0$ showing the evolution of the influence zones χ_-, χ_+ of the slow (v_-) and fast (v_+) wave speeds as a function of time τ

[3] For hyperelastic material, a linearization of perturbation yields $\Delta N_{\alpha\beta} = \mathcal{L}_{\alpha\beta\gamma\delta}\Delta F_{\gamma\delta}$. To avoid algebraic complications we further assume that the same holds true for a rate-independent material.

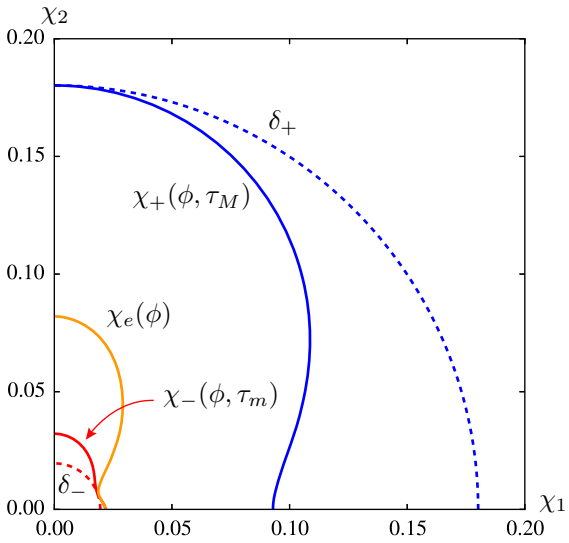

Fig. 4 Influence zones of an initial ($\tau = 0$) perturbation at $\mathbf{X} = 0$ for biaxially stretched thin, flat plates: $\chi_-(\phi, \tau_m)$, $\chi_+(\phi, \tau_M)$ in *solid lines*. The minimum δ_- and maximum δ_+ discs of influence are depicted in *dotted line*. Also plotted in *dashed line* is $\chi_e(\phi)$, the locus of points reached by the wave propagating along a given direction ϕ until loss of ellipticity occurs. Results correspond to uniaxial strain $\psi = 0$ of a power-law type material with hardening exponent $n = 0.22$

as shown in Fig. 4. Two particular values of $\tau_e(\phi)$ are of interest: the ones corresponding to the lowest (τ_m) and highest (τ_M) values of $\tau_e(\phi)$ with respect to ϕ, namely:

$$\tau_m = \min_{\phi} \tau_e(\phi) = \tau_e(\phi_m) \; ;$$
$$\tau_M = \max_{\phi} \tau_e(\phi) = \tau_e(\phi_M) \; . \tag{2.11}$$

At time τ_m the plate reaches for the first time conditions of loss of ellipticity of its incremental equilibrium equations. The influence zone corresponding to the lowest speed v_- is $\chi_-(\phi, \tau_m)$ as seen in Fig. 4. One can thus define δ_- the radius of the minimum disc influenced by the perturbation at $\mathbf{X} = \mathbf{0}$ at the onset of loss of ellipticity:

$$\delta_- = \chi_-(\phi_m, \tau_m) = \int_0^{\tau_m} v_-\left(\phi_m, \tau'\right) d\tau' \; . \tag{2.12}$$

In a similar way we are interested in the maximum size disc, centered at $\mathbf{X} = \mathbf{0}$, that the perturbation can reach. At time τ_M the plate has already lost ellipticity for all possible directions of wave propagation ϕ and the zone influenced by the perturbation at $\mathbf{X} = \mathbf{0}$ is $\chi_+(\phi, \tau_M)$ as seen in Fig. 4. In analogy to δ_-, one can also define δ_+ the radius of the maximum disc covering entirely the range of influence of the perturbation at $\mathbf{X} = \mathbf{0}$ when the plate has lost ellipticity along all possible directions ϕ, namely:

$$\delta_+ = \chi_+(\phi_M, \tau_M) = \int_0^{\tau_M} v_+\left(\phi_M, \tau'\right) d\tau' \; . \tag{2.13}$$

It should be noted here that δ_- exists as long as the model loses ellipticity for the loading considered. Moreover even if a δ_- exists, a δ_+ might not.

2.2 Numerical calculations

Nonlinear dynamics calculations for the evolution of a spatially localized initial perturbation are done using the finite element method using the simplest constitutive law, namely a hyperelastic, finite (logarithmic) strain model fitted a uniaxial power law. The use of this model for elastoplastic materials is justified by the absence of unloading in the calculations (of interest is the response of the plate up to the loss of ellipticity). A brief description of the algorithm used is presented here.

The starting point of the calculations is the weak formulation of equilibrium equations (2.2) in Lagrangian (reference) configuration:

$$\int_A [N_{\alpha\beta}\delta u_{\alpha,\beta} + \rho_0 \frac{\partial^2 u_\alpha}{\partial t^2}\delta u_\alpha] dA = 0 \; , \tag{2.14}$$

with $\delta\mathbf{u}$ is the test function. A spatial FEM discretization leads to the solution of the following system of equations:

$$\mathbf{M} \cdot \mathbf{A}(t) + \mathbf{F}(\mathbf{U}(t)) = \mathbf{0} \; ; \quad \mathbf{A}(t) \equiv \partial \mathbf{V}(t)/\partial t \; ,$$
$$\mathbf{V}(t) \equiv \partial \mathbf{U}(t)/\partial t \tag{2.15}$$

where $\mathbf{F}$ is the force vector, $\mathbf{M}$ the mass matrix and $\mathbf{U}(t)$, $\mathbf{V}(t)$ and $\mathbf{A}(t)$ respectively vector of nodal displacements, velocities and accelerations.

The time marching algorithm chosen for the solution of (2.15) is the HHT-α method (see Hilber et al. (1977) which uses the following updating scheme for the displacement and velocity vectors:

$$\begin{aligned}\mathbf{U}^{t+\Delta t} &= \mathbf{U}^t + \Delta t\mathbf{V}^t \\ &\quad + \frac{(\Delta t)^2}{2}\left((1-2\beta)\mathbf{A}^t + 2\beta\mathbf{A}^{t+\Delta t}\right) , \\ \mathbf{V}^{t+\Delta t} &= \mathbf{V}^t + \Delta t\left((1-\gamma)\mathbf{A}^t + \gamma\mathbf{A}^{t+\Delta t}\right) , \end{aligned} \tag{2.16}$$

which are in turn used for the iterative solution of (2.15) by driving its residual vector $\mathbf{R}$ at each time step to zero according to:

$$\mathbf{0} = \mathbf{R}^{t+\Delta t} = \mathbf{M}\cdot\mathbf{A}^{t+\Delta t} + (1+\alpha)\mathbf{F}(\mathbf{U}^{t+\Delta t}) - \alpha\mathbf{F}(\mathbf{U}^t) . \tag{2.17}$$

In the above expressions, the constants α, β and γ govern the stability and numerical dissipation of the algorithm and are related by $\beta = (1-\alpha)^2/4$ and $\gamma = 1/2 - \alpha$ (see Hilber et al. 1977). For the calculations reported here we choose $\alpha = -0.05$. The remainder $\mathbf{R}_i^{t+\Delta t}$ at iteration i at time step $t+\Delta t$ is updated using the tangent stiffness matrix $\mathbf{K}_i^{t+\Delta t}$ of the algorithm:

$$\begin{aligned}\mathbf{R}_i^{t+\Delta t} &= \mathbf{K}_i^{t+\Delta t}\cdot(\mathbf{U}_{i+1}^{t+\Delta t} - \mathbf{U}_i^{t+\Delta t}) , \\ \mathbf{K}_i^{t+\Delta t} &\equiv \frac{\partial\mathbf{R}}{\partial\mathbf{U}_i^{t+\Delta t}} = \frac{1}{\beta\Delta t^2}\mathbf{M} + (1+\alpha)\frac{\partial\mathbf{F}}{\partial\mathbf{U}}(\mathbf{U}_i^{t+\Delta t}) , \end{aligned} \tag{2.18}$$

until convergence in the displacement is reached, i.e. $\|\mathbf{U}_{i+1}^{t+\Delta t} - \mathbf{U}_i^{t+\Delta t}\| \le \epsilon\|\mathbf{U}_i^{t+\Delta t}\|$, where ϵ is a conveniently chosen tolerance parameter.

The spatial discretization of the plate uses standard 2D isoparametric quadrilateral elements. The boundary conditions imposed at any time are the displacements and velocities of the principal (perfect) solution given in (2.1). The reference configuration rectangular domain used in the calculations covers completely a disc of radius δ_+, thus ensuring that no perturbation wave ever reaches any boundary. The initial conditions are the displacements and velocities of the principal solution. Instead of prescribing a slightly perturbed initial displacement or velocity field, we chose the equivalent approach of using an initial imperfection through a central element with a slightly lower shear modulus, as detailed in the results section. A special element incorporating the constitutive law and time solution algorithm described here is then introduced into a commercial FEM code (ABAQUS) to calculate the results for this work.

3 Results

This section starts with the constitutive models chosen. It continues with the study of the evolution of a single spatially localized perturbation with different amplitudes, followed by the study on interactions of such perturbations. These results show the stability of the biaxially strained plate, as long as none of its points has reached the loss of ellipticity condition and determine the actual (nonlinear) zone of influence of the perturbation. The section concludes by investigating the influence of constitutive law and load orientation on the size of the minimum and maximum influence zones.

3.1 Constitutive laws

The analysis presented in Sect. 2 is general; any rate-independent constitutive law (which can be put in the form of (2.3)) can be accommodated, provided that its membrane (plane stress) version loses ellipticity at some strain level. Results presented here correspond to the three such models: a hyperelastic (deformation theory) type model of plasticity, the J_2 deformation theory model of Stören and Rice (1975) and a finite strain generalization of the J_2 flow theory. All models are fitted to the same power law uniaxial stress-strain curve and share the same principal solution. Since no unloading occurs in the perturbed plate prior to reaching a loss of ellipticity, the use of deformation theory type constitutive models is adequate for analyzing its stability.

We start with the hyperelastic constitutive model, which is described by a strain energy W, a function of the equivalent logarithmic strain ϵ_e as follows:

$$W = E(\epsilon_y)^2\left[\frac{1}{1+\chi}\left(\frac{\epsilon_e}{\epsilon_y}\right)^{\chi+1} + \frac{1}{2}\left(\frac{\chi-1}{\chi+1}\right)\right] ,$$

$$\begin{cases} \chi = 1 \text{ for } \epsilon_e \le \epsilon_y , \\ \chi = n \text{ for } \epsilon_e > \epsilon_y , \end{cases} \tag{3.1}$$

where the *equivalent strain* ϵ_e is given in terms of the principal logarithmic strain components ϵ_α:

$$\epsilon_e = \frac{2}{\sqrt{3}}\left[\epsilon_1^2 + \epsilon_2^2 + \epsilon_1\epsilon_2\right]^{1/2}; \ \epsilon_\alpha = \ln\lambda_\alpha , \tag{3.2}$$

with λ_i the stretch ratios of the deformation (principal values of the stretch tensor $\mathbf{U}$, the rotationless part of the deformation gradient $\mathbf{F} = \mathbf{R} \cdot \mathbf{U}$; $\mathbf{U} = \left(\mathbf{F}^T \cdot \mathbf{F}\right)^{1/2}$).

The above isotropic model is fitted with a piecewise power law uniaxial stress-strain curve[4]:

$$\frac{\sigma_e}{\sigma_y} = \left(\frac{\epsilon_e}{\epsilon_y}\right)^{\chi} , \tag{3.3}$$

where the exponent χ is given in (3.1) and the *equivalent stress* σ_e is the Von-Mises stress given in terms of the principal Cauchy stress σ_α by:

$$\sigma_e = \left(\sigma_1^2 + \sigma_2^2 - \sigma_1\sigma_2\right)^{1/2} . \tag{3.4}$$

Since the principal solution is biaxial straining, the principal stresses are related to the principal logarithmic strains by:

$$\begin{aligned} &\sigma_\alpha = \frac{\partial W}{\partial \epsilon_\alpha} \; ; \quad \sigma_1 = \frac{2}{3} E_s \left(2\epsilon_1 + \epsilon_2\right) , \\ &\sigma_2 = \frac{2}{3} E_s \left(\epsilon_1 + 2\epsilon_2\right) , \end{aligned} \tag{3.5}$$

where $E_s = \sigma_e/\epsilon_e$ is the *secant modulus*, $E_t = d\sigma_e/d\epsilon_e$ is the *tangent modulus* of the equivalent uniaxial stress-strain curve in which the equivalent stress and strain are related by: $\sigma_e = dW/d\epsilon_e$.

When we are no longer along the principal axes of deformation (as is the case of numerical FEM calculations) the stress measures and incremental moduli of this model (see (2.3)) are found by:

$$N_{\alpha\beta} = \frac{\partial W}{\partial F_{\alpha\beta}}, \quad \mathcal{L}_{\alpha\beta\gamma\delta} = \frac{\partial^2 W}{\partial F_{\alpha\beta} F_{\gamma\delta}}. \tag{3.6}$$

In addition to the above-presented hyperelastic constitutive model used in numerical calculations, for comparison purposes two more constitutive models will be employed for the calculation of influence zones under different loading orientations: the J_2 deformation theory model by Stören and Rice (1975) and the J_2 flow theory model, both in their finite strain version.

As previously mentioned, all three constitutive models share the same uniaxial stress-strain curve and are so constructed as to have the same response when loaded with fixed principal axes of deformation. Since the calculation of δ_- and δ_+ (the minimum and maximum) influence disc sizes for the different constitutive laws requires the principal solution, the evaluation of the corresponding incremental moduli are presented below along the fixed principal axes.

The non-zero components of the plane stress moduli in (2.3) are given below in two groups; the *normal moduli* components are:

$$\begin{aligned} \mathcal{L}_{1111} &= \frac{1}{\lambda_1^2}\left[\frac{4}{3}E^* + \left(E_t - E^*\right)\left(\frac{\sigma_1}{\sigma_e}\right)^2 - \sigma_1\right] , \\ \mathcal{L}_{1122} &= \frac{1}{\lambda_1\lambda_2}\left[\frac{2}{3}E^* + \left(E_t - E^*\right)\frac{\sigma_1\sigma_2}{\sigma_e^2}\right] , \\ \mathcal{L}_{2222} &= \frac{1}{\lambda_2^2}\left[\frac{4}{3}E^* + \left(E_t - E^*\right)\left(\frac{\sigma_2}{\sigma_e}\right)^2 - \sigma_2\right] , \end{aligned} \tag{3.7}$$

where for the J_2 deformation theory model as well as the hyperelastic model in (3.1), (3.2) the normal incremental moduli are the same with $E^* = E_s = \sigma_e/\epsilon_e$ while for the J_2 flow theory model $E^* = E$.

The *shear moduli* components are given by:

$$\begin{aligned} \mathcal{L}_{1212} &= \frac{1}{\lambda_2^2}\left[\frac{E^*}{3} + \frac{\sigma_2 - \sigma_1}{2}\right] , \\ \mathcal{L}_{2121} &= \frac{1}{\lambda_1^2}\left[\frac{E^*}{3} + \frac{\sigma_1 - \sigma_2}{2}\right] , \\ \mathcal{L}_{1221} &= \mathcal{L}_{2112} = \frac{1}{\lambda_1\lambda_2}\left[\frac{E^*}{3} - \frac{\sigma_1 + \sigma_2}{2}\right] , \end{aligned} \tag{3.8}$$

where for the J_2 flow theory $E^* = E$, for the J_2 deformation theory $E^* = E_s$ while for the hyperelastic model $E^* = E_s[(\lambda_1^2 + \lambda_2^2)/(\lambda_1^2 - \lambda_2^2)](\ln\lambda_1 - \ln\lambda_2)$. The principal stresses σ_α for all three models are identical and given by (3.5).

The hyperelastic and J_2 deformation theory models lose ellipticity at realistic strain levels for all load path orientations ψ (see definition (2.1)) while the J_2 flow theory gives unrealistic results for load orientations $\psi > 0$ (and hence the need for the deformation theory models used). Moreover, only values of ψ for which both principal stresses σ_i are tensile ($\sigma_\alpha = \partial W/\partial\epsilon_\alpha > 0$) will be investigated, since a compressible membrane stress is unsustainable (thin plate will immediately buckle).

[4] For a uniaxial stress state $\epsilon_2 = -\epsilon_1/2$ and $\epsilon_e = \epsilon$; Moreover ϵ_y and $\sigma_y = E\epsilon_y$ are the yield strain and stress respectively in a uniaxial loading path.

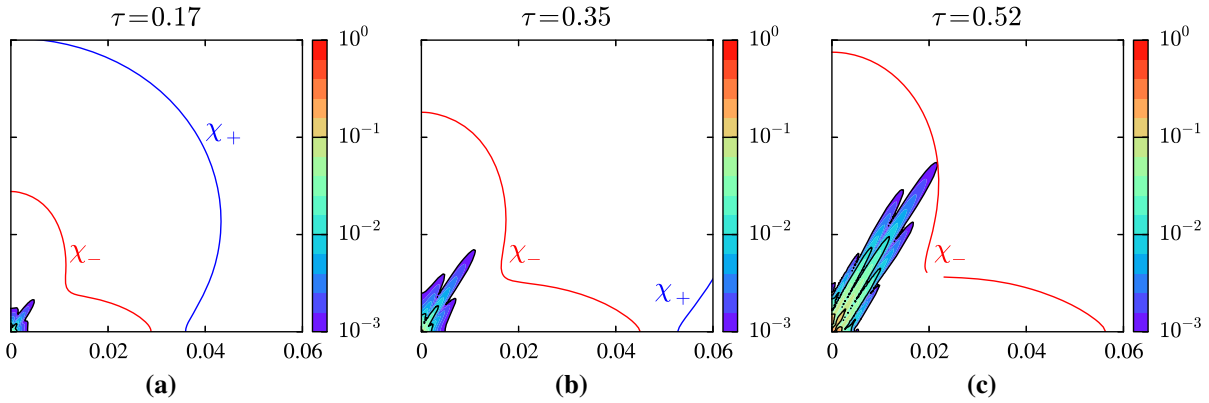

Fig. 5 Green-Lagrange strain perturbation contours $\Delta E(\boldsymbol{\chi}, \tau)$ at three different dimensionless times (**a**) $\tau = 0.17$, (**b**) $\tau = 0.35$ and (**c**) $\tau = 0.52 = \tau_m$, where only *contours* of $\Delta E \geq 10^{-3}$ are shown in *color*. The extent of the influence zones $\chi_-(\phi, \tau)$ and $\chi_+(\phi, \tau)$ for the slowest and fastest wave speeds v_- and v_+ respectively, are also shown in these figures. Results correspond to a hyperelastic constitutive law with a piecewise power law *uniaxial curve* ($\epsilon_y = 0.002$, $n = 0.22$) and a loading angle $\tan\psi = -1/2$

3.2 Evolution at a spatially localized perturbation

We start by analyzing the influence of an initial imperfection, located at the origin, in the form of a square domain of size $\Delta\chi = 6 \times 10^{-5}$ whose shear modulus is $G(1 + \xi)$, where $\xi = 4$ is the imperfection amplitude. Equivalently, one could have taken a perturbation in the principal solution (dimensionless) displacement field $u_1(\boldsymbol{\chi}, 0) = \chi_1 \tau \cos\psi$, $u_2(\boldsymbol{\chi}, 0) = \chi_2 \tau \sin\psi$ or in the principal solution (dimensionless) velocity field $v_1(\boldsymbol{\chi}, 0) = \chi_1 \cos\psi$, $v_2(\boldsymbol{\chi}, 0) = \chi_2 \sin\psi$. The shear modulus imperfection used here is equivalent to an isotropic displacement or velocity field perturbation that would have resulted from a sudden isotropic dilation/contraction of the perturbed domain at $\tau = 0$. Hence we use the terms initial imperfection or perturbation indistinguishably.

To better visualize the influence of the initial perturbation on the dynamic behavior of the biaxially strained plate, we plot two different measures of the perturbations: the perturbation in the total Green-Lagrange strain:

$$\begin{aligned} \Delta E &\equiv \left\| \mathbf{E}(\boldsymbol{\chi}, \tau) - \mathbf{E}^0(\boldsymbol{\chi}, \tau) \right\| \\ &= \left[\left(E_{\alpha\beta} - E^0_{\alpha\beta}\right)\left(E_{\alpha\beta} - E^0_{\alpha\beta}\right) \right]^{1/2} > 0 \,, \\ E_{\alpha\beta} &= \frac{1}{2}\left(F_{\gamma\alpha} F_{\gamma\beta} - \delta_{\alpha\beta}\right); \\ E^0_{\alpha\beta} &= \operatorname{diag}\left[\frac{1}{2}\left(\left(\lambda_\gamma\right)^2 - 1 \right) \right] , \end{aligned} \tag{3.9}$$

and the perturbation in the shear component of the Green-Lagrange strain, which in view of the absence of a shear strain component in the principal solution, is the shear strain component of the perturbed solution:

$$\Delta E_{12} \equiv \left| E_{12}(\boldsymbol{\chi}, \tau) - E^0_{12}(\boldsymbol{\chi}, \tau) \right| = \left| E_{12} \right| > 0 \,. \tag{3.10}$$

The influence of the initial perturbation is shown in Figs. 5 and 6 which depict the evolution of contours of ΔE and ΔE_{12} in $[\chi_1, \chi_2]$ space (only the positive quadrant is shown here due to symmetry). More specifically, the evolution of the strain perturbation due to an initial imperfection of amplitude $\xi = 4$ (contours of perturbations with magnitudes below 10^{-3} are not plotted, for visual enhancement of the evolution of the initial perturbation) for three different dimensionless times τ ($0.17, 0.35$ and $0.52 = \tau_m$) are depicted in these figures. Results correspond to a hyperelastic material with $n = 0.22$ and $\epsilon_y = 10^{-3}$, strained along a loading path with $\psi = -1/2$, which corresponds to uniaxial stressing for small strains.

For the lowest value of $\tau = 0.17$, only a small region near the origin $\chi = 0$ is affected, while for $\tau = 0.35$ the emergence of a localized band of deformation in the direction of the loss of ellipticity of the material ($\pi/2 - \phi_m$) is obvious. At the time of onset of loss of ellipticity, τ_m the localized deformation band in the direction $\pi/2 - \phi_m$ is more pronounced. What is worth mentioning is that the localized deformation appears

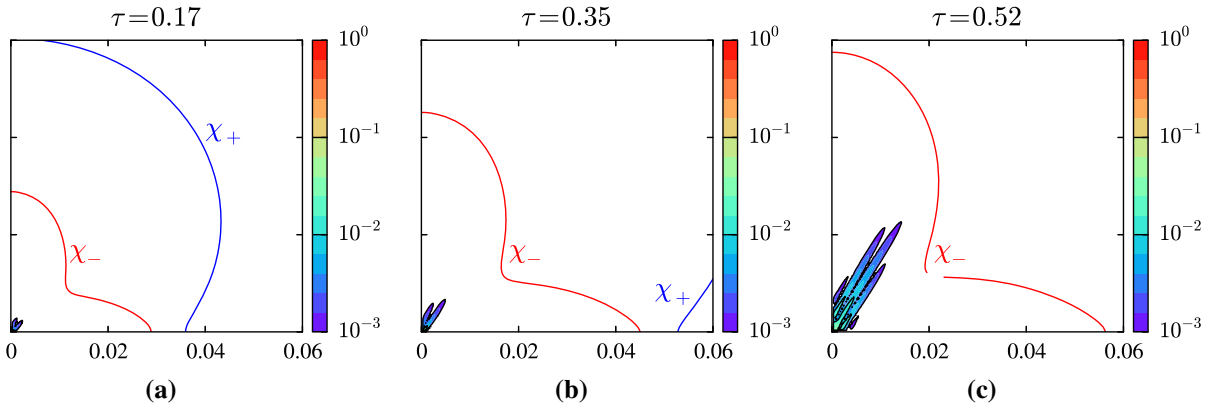

Fig. 6 Shear strain perturbation contours $\Delta E_{12}(\chi, \tau)$ at three different dimensionless times (**a**) $\tau = 0.17$, (**b**) $\tau = 0.35$ and (**c**) $\tau = 0.52 = \tau_m$, where only *contours* of $\Delta E \geq 10^{-3}$ are shown in *color*. The extent of the influence zones $\chi_-(\phi, \tau)$ and $\chi_+(\phi, \tau)$ for the slowest and fastest wave speeds v_- and v_+ respectively, are also shown in these figures. Results correspond to a hyperelastic constitutive law with a piecewise power law *uniaxial curve* ($\epsilon_y = 0.002$, $n = 0.22$) and a loading angle $\tan\psi = -1/2$

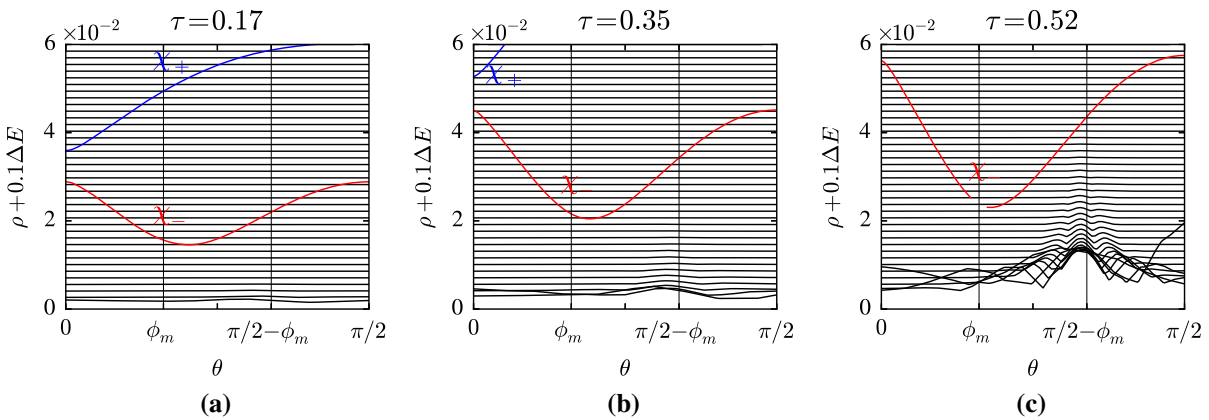

Fig. 7 Green-Lagrange strain perturbation ΔE plotted in polar coordinates $(\chi_1, \chi_2) = (\rho\cos\theta, \rho\sin\theta)$ for $\theta \in [0, \pi/2]$ and at different distances ρ from the origin (distance is increasing by constant $\Delta\rho = 1.5 \times 10^{-3}$ and $\rho + \Delta E(\rho, \theta)$ is plotted in the *y-axis*). Results are shown for three different dimensionless times (**a**) $\tau = 0.17$, (**b**) $\tau = 0.35$ and (**c**) $\tau = 0.52 = \tau_m$. The extent of the influence zones $\chi_-(\tau)$ and $\chi_+(\tau)$ for the slowest and fastest wave speeds v_- and v_+ respectively are also shown in these figures. Results correspond to a hyperelastic constitutive law with a piecewise power law *uniaxial curve* ($\epsilon_y = 0.002$, $n = 0.22$) and a loading angle $\tan\psi = -1/2$

to propagate in three *tongues*. This phenomenon can be explained by the square shape of the initial perturbation domain, where each corner acts as a *source*. A static analogue of this phenomenon has been found in Abeyaratne and Triantafyllidis (1981). Moreover the width of the localized deformation zone is considerably larger than the size of the initial perturbation due to the propagation of the signal.

Notice that results in Fig. 5 are similar to those of Fig. 6, save for the lower values of the perturbation in the latter compared to the former figure—compared for the same time—due to the different norm used (the norm used in Fig. 5 contains perturbations of all strain components).

A different way to depict the propagation of perturbation initiated at $\chi = 0$ is presented in polar coordinates in Figs. 7 and 8 which shows respectively ΔE and ΔE_{12} as function of the polar angle θ at different positions ρ incremented by $\Delta\rho = 1.5 \times 10^{-3}$ from the center ($\chi_1 = \rho\cos\psi$, $\chi_2 = \rho\sin\psi$), for the same material and loading path and at the same three times as in Figs. 5 and 6. Notice that as time approaches the critical value τ_m a localized deformation pattern appears with maximum at about $\theta = \pi/2 - \phi_m$ (the strain

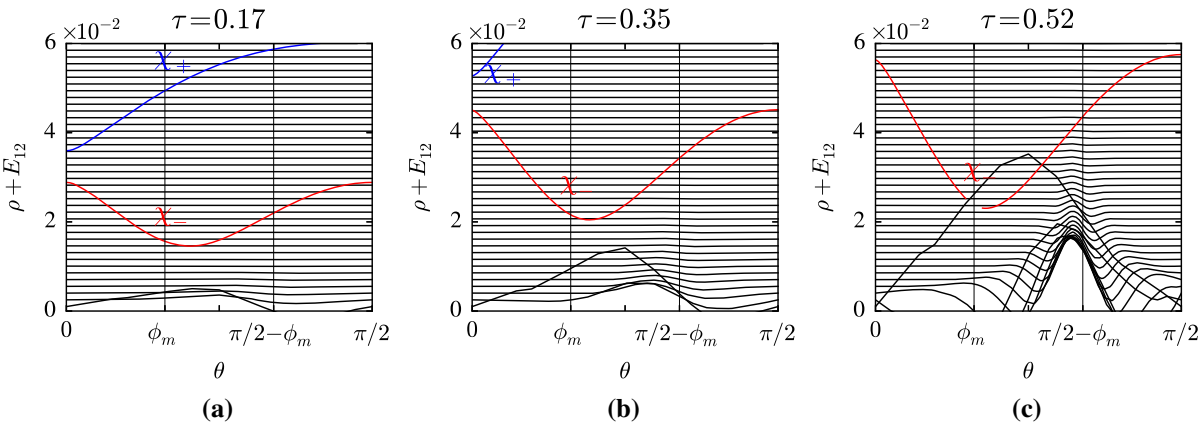

Fig. 8 Shear strain perturbation ΔE_{12} plotted in polar coordinates $(\chi_1, \chi_2) = (\rho\cos\theta, \rho\sin\theta)$ for $\theta \in [0, \pi/2]$ and at different distances ρ from the origin (distance is increasing by constant $\Delta\rho = 1.5 \times 10^{-3}$ and $\rho + \Delta E(\rho, \theta)$ is plotted in the *y-axis*). Results are shown for three different dimensionless times (**a**) $\tau = 0.17$, (**b**) $\tau = 0.35$ and (**c**) $\tau = 0.52 = \tau_m$. The extent of the influence zones $\chi_-(\tau)$ and $\chi_+(\tau)$ for the slowest and fastest wave speeds v_- and v_+ respectively are also shown in these figures. Results correspond to a hyperelastic constitutive law with a piecewise power law *uniaxial curve* ($\epsilon_y = 0.002$, $n = 0.22$) and a loading angle $\tan\psi = -1/2$

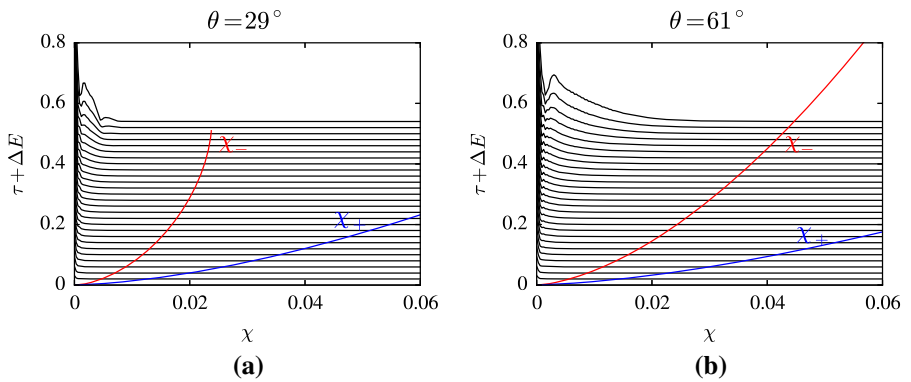

Fig. 9 Profile of Green-Lagrange strain perturbation ΔE plotted at different dimensionless times $0 \le \tau \le \tau_m$ (in increments of $\Delta\tau = 0.02$) at a distance ρ from the origin and for two different values of polar angle (**a**) $\theta = \phi_m$ and (**b**) $\theta = \pi/2 - \phi_m$. The extent of the influence zones $\chi_-(\tau)$ and $\chi_+(\tau)$ for the slowest and fastest wave speeds v_- and v_+ respectively are also shown in these figures. Results correspond to a hyperelastic constitutive law with a piecewise power law *uniaxial curve* ($\epsilon_y = 0.002$, $n = 0.22$) and a loading angle $\tan\psi = -1/2$

discontinuity at the loss of ellipticity appears in a line perpendicular to the critical direction **n**, which forms an angle ϕ_m with the χ_1 axis).

A better way to visualize the size of the localized deformation zone is by plotting the time evolution $0 \le \tau \le \tau_m$ of perturbation as a function of dimensionless distance from the origin for two different values of θ: $29° = \pi/2 - \phi_m$ and $61° = \phi_m$. The results for ΔE and ΔE_{12} are depicted, respectively in Figs. 9 and 10. The blue lines give the influence cone of v_+ while the red lines give the influence cone of v_-. Notice the pattern of the different tongues of the localization zone evolving with time, as expected from Figs. 5 and 6.

These results show that, due to wave propagation, the width of the localized deformation zones are considerably larger than the width of the initial imperfection, but also a fraction of the linearized estimate χ_- (influence zone for the slower wave) for the same time, a phenomenon also observed for the growth of a localized perturbation in the nonlinear bar model of Ravi-Chandar and Triantafyllidis (2015).

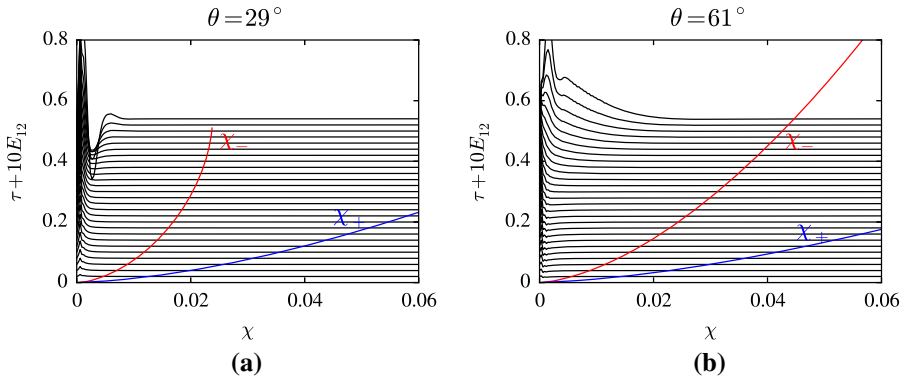

Fig. 10 Profile of shear strain perturbation ΔE_{12} plotted at different dimensionless times $0 \leq \tau \leq \tau_m$ (in increments of $\Delta\tau = 0.02$) at a distance ρ from the origin and for two different values of polar angle (**a**) $\theta = \phi_m$ and (**b**) $\theta = \pi/2 - \phi_m$. The extent of the influence zones $\chi_-(\tau)$ and $\chi_+(\tau)$ for the slowest and fastest wave speeds v_- and v_+ respectively are also shown in these figures. Results correspond to a hyperelastic constitutive law with a piecewise power law *uniaxial curve* ($\epsilon_y = 0.002$, $n = 0.22$) and a loading angle $\tan\psi = -1/2$

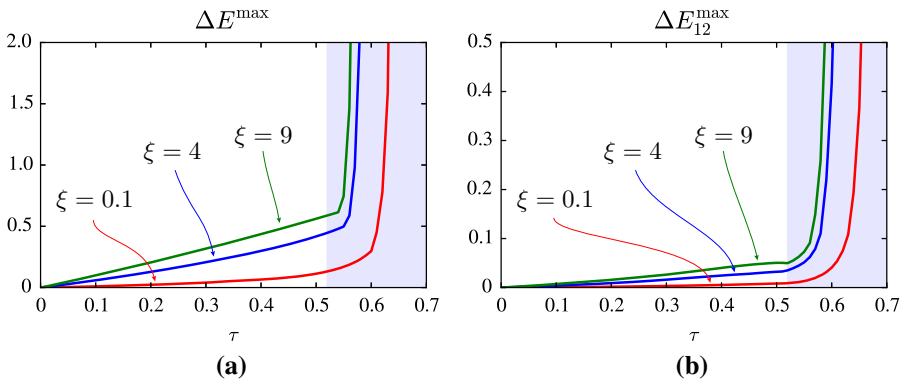

Fig. 11 Influence of the initial amplitude ξ of a localized perturbation at $\chi = 0$. Notice that the magnitude of the perturbation (measured by its maximum, at a given time τ, over the entire plate, i.e. $\Delta E^{\max}(\tau) \equiv \max_{\boldsymbol{\chi}\in\mathbb{R}^2} \Delta E(\boldsymbol{\chi}, \tau)$ in (**a**) and $\Delta E_{12}^{\max}(\tau) \equiv \max_{\boldsymbol{\chi}\in\mathbb{R}^2} \Delta E_{12}(\boldsymbol{\chi}, \tau)$ in (**b**)) decreases, for each value of $\tau < \tau_m$, with decreasing ξ, thus showing the stability of the structure as long as it stays in the elliptic domain (non-shaded area $\tau < \tau_m$ in the *graphs*). Results correspond to a hyperelastic constitutive law with a piecewise power law *uniaxial curve* ($\epsilon_y = 0.002$, $n = 0.22$) and a loading angle $\tan\psi = -1/2$

To study the stability of the structure under a spatially localized perturbation, we follow the time evolution of the maximum (over the entire domain $\mathbb{R}^2$) perturbations $\Delta E^{\max}(\tau) \equiv \max_{\boldsymbol{\chi}\in\mathbb{R}^2} \Delta E(\boldsymbol{\chi}, \tau)$ and $\Delta E_{12}^{\max}(\tau) \equiv \max_{\boldsymbol{\chi}\in\mathbb{R}^2} \Delta E_{12}(\boldsymbol{\chi}, \tau)$ in Fig. 11.

Notice that for $\tau < \tau_m$ the two perturbation norms decrease as a function of time with decreasing initial amplitude, showing the stability of the structure for times prior to the loss of ellipticity (the ellipticity domain $\tau > \tau_m$ is indicated by the shaded area in the above figures). A similar result has been obtained for the 1D nonlinear bar model by Ravi-Chandar and Triantafyllidis (2015), who find the stability of spatially localized perturbations at all times prior to reaching the bar's Considère point (maximum force).

All the above calculations correspond to a strain path with a loading angle $\tan\psi = -1/2$ (i.e. uniaxial stressing at small strains). It is of interest to present results for different loading angles and we choose to show the influence of the same localized at $\boldsymbol{\chi} = \mathbf{0}$ initial perturbation (initial imperfection of amplitude $\xi = 4$) and the same material (a hyperelastic constitutive law with a piecewise power law uniaxial curve $\epsilon_y = 0.002$, $n = 0.22$) in a biaxially strained plate with $\tan\psi = 0$ in Fig. 12 and with $\tan\psi = 0$ in Fig. 13. Results in these figures depict the evolution of shear strain ΔE_{12}

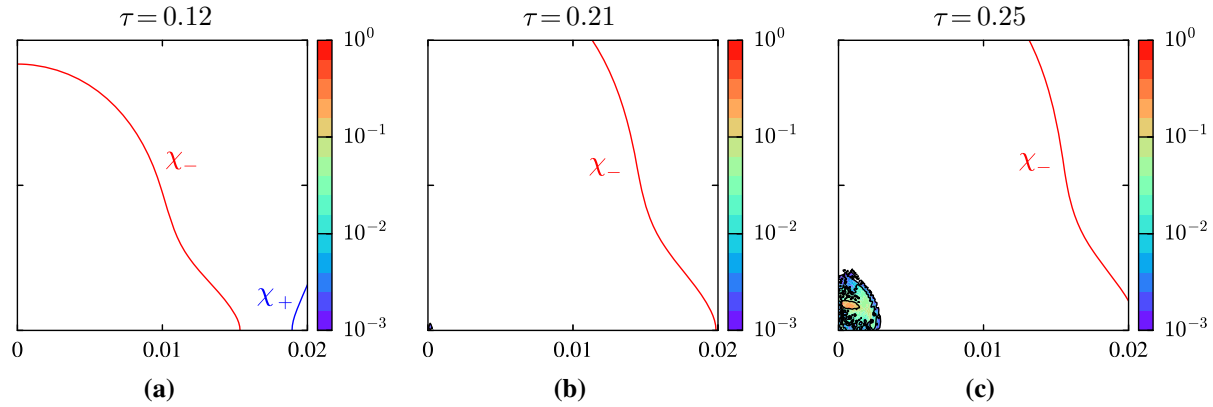

Fig. 12 Shear strain perturbation contours $\Delta E_{12}(\chi, \tau)$ at three different dimensionless times (**a**) $\tau = 0.12$, (**b**) $\tau = 0.21$ and (**c**) $\tau = 0.25 = \tau_m$, where only *contours* of $\Delta E \geq 10^{-3}$ are shown in *color*. The extent of the influence zones $\chi_-(\phi, \tau)$ and $\chi_+(\phi, \tau)$ for the slowest and fastest wave speeds v_- and v_+ respectively, are also shown in these figures. Results correspond to a hyperelastic constitutive law with a piecewise power law *uniaxial curve* ($\epsilon_y = 0.002$, $n = 0.22$) and a loading angle $\tan\psi = 0$

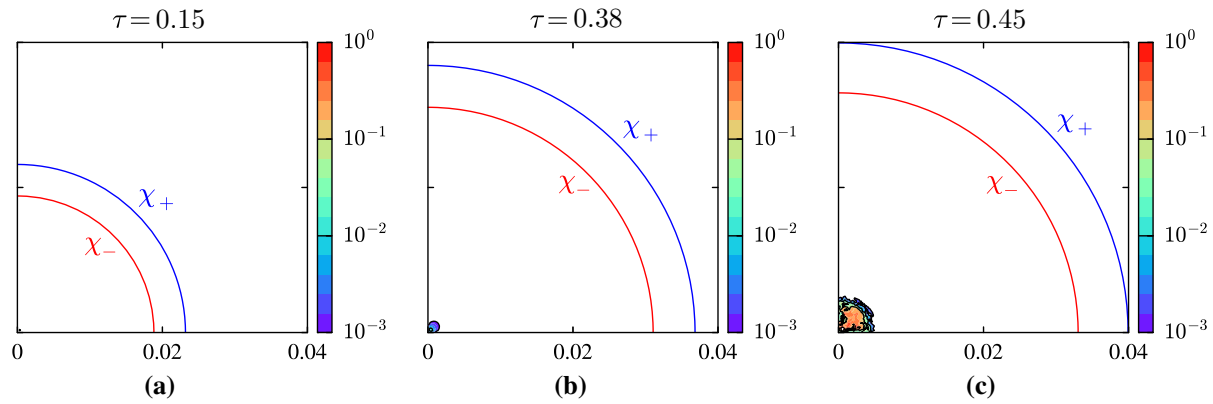

Fig. 13 Shear strain perturbation contours $\Delta E_{12}(\chi, \tau)$ at three different dimensionless times (**a**) $\tau = 0.15$, (**b**) $\tau = 0.38$ and (**c**) $\tau = 0.45 = \tau_m$, where only *contours* of $\Delta E \geq 10^{-3}$ are shown in *color*. The extent of the influence zones $\chi_-(\phi, \tau)$ and $\chi_+(\phi, \tau)$ for the slowest and fastest wave speeds v_- and v_+ respectively, are also shown in these figures. Results correspond to a hyperelastic constitutive law with a piecewise power law *uniaxial curve* ($\epsilon_y = 0.002$, $n = 0.22$) and a loading angle $\tan\psi = 1$

contours in $[\chi_1, \chi_2]$ space (only the positive quadrant is shown here due to symmetry).

More specifically, for $\tan\psi = 0$ the evolution of the shear strain ΔE_{12} due to a localized initial perturbation at the origin (contours of perturbations with magnitudes below 10^{-3} are not plotted, for visual enhancement of the evolution of the initial perturbation) for three different dimensionless times τ (0.12, 0.21 and $0.25 = \tau_m$) are depicted in Fig. 12. Results correspond to a hyperelastic material with $n = 0.22$ and $\epsilon_y = 10^{-3}$. For this loading path, one finds that the corresponding angle at the loss of ellipticity $\phi_m = 0$, i.e. the characteristic direction at the onset of the loss of ellipticity is the χ_2 axis. Consequently, the localization of deformation spreads more along this axis, as one can see in Fig. 12c.

For the case of balanced biaxial stretching, $\tan\psi = 1$, the evolution of the shear strain ΔE_{12} due to an localized initial perturbation at the origin for three different dimensionless times τ (0.15, 0.38 and $0.45 = \tau_m$) are depicted in Fig. 13. Results correspond to a hyperelastic material with $n = 0.22$ and $\epsilon_y = 10^{-3}$. Due to the in-plane isotropy of the loading, for this loading path the corresponding angle at the loss of ellipticity ϕ_m is indeterminate and hence any direction can be a characteristic one. Moreover the influence zones $\chi_-(\phi, \tau)$ and $\chi_+(\phi, \tau)$ for the slowest and fastest wave speeds

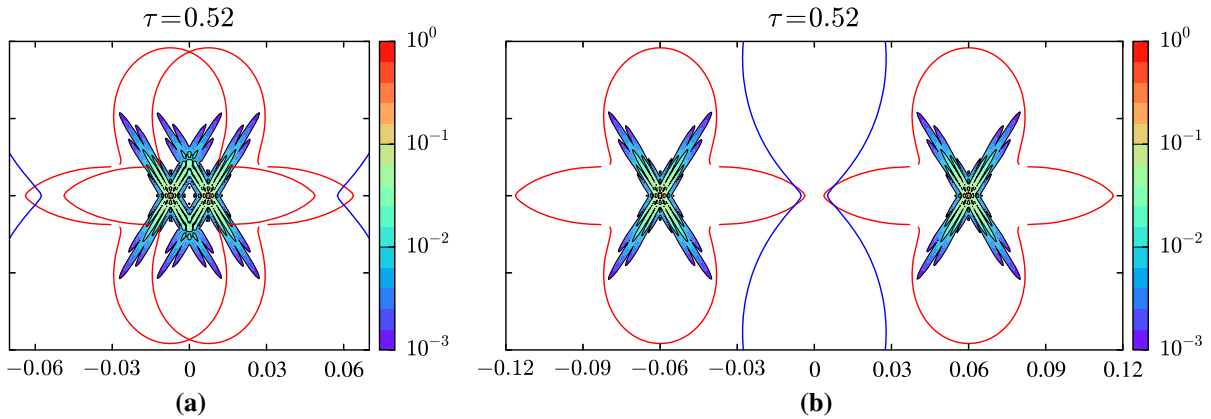

Fig. 14 Interaction of same amplitude perturbations initially at a distance (**a**) $h < \delta_-$ and (**b**) $h > \delta_+$. Results show contours of strain perturbation $\Delta E \geq 10^{-3}$ calculated at the time of loss of ellipticity $\tau_m = 0.52$ and corresponding to a hyperelastic constitutive model with a piecewise power law *uniaxial curve* ($\epsilon_y = 0.002$, $n = 0.22$) and a loading angle $\tan\psi = -1/2$

ν_- and ν_+ respectively, are concentric circles, as one can see in Fig. 13. The localized deformation zones also appear to grow uniformly in each direction; the deviation from the perfect disc shape is attributed to the rectangular shape of the initial imperfection.

3.3 Size of influence zones for various constitutive laws and loading orientations

In Sect. 2 we have introduced the minimum δ_- and maximum δ_+ influence disc sizes (see 2.12 and 2.13). This information is useful in determining initial spacing of perturbations that will or will not interact, since in actual structures one expects a multitude of statistically distributed defects. To illustrate this point we consider the interaction of two defects in Fig. 14 that shows contours of strain perturbation $\Delta E \geq 10^{-3}$ at the time of loss of ellipticity τ_m in a plate with two localized imperfections of the same size and initial amplitude spaced at a distance smaller than δ_- in a) and at distance larger than δ_- in b).

It appears from Fig. 14a, that when the localized deformation zones of the two perturbations meet and interact, the width of the resulting localized deformation zone is bigger than the width of the single localized imperfection. The failure pattern for the stretched plate can be explained as resulting from interaction of statistically distributed such localized defects—inevitable in reality—as observed experimentally in the tube expansion experiments of Zhang and Ravi-Chandar (2010).

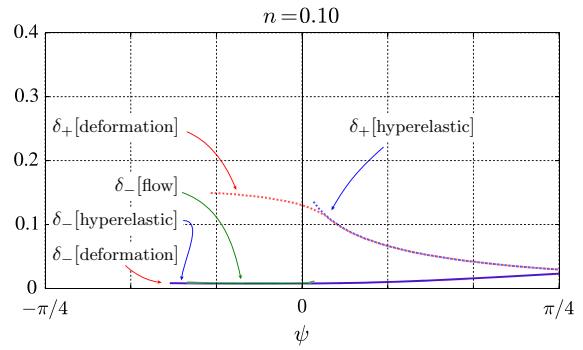

Fig. 15 Minimum δ_- and maximum δ_+ influence disc sizes, in *dashed* and *solid lines* respectively, as functions of the load orientation angle ψ for the three different constitutive models considered, all sharing the same uniaxial *stress-strain curve* with $\epsilon_y = 0.002$, $n = 0.1$

The size of minimum δ_- and maximum δ_+ influence discs, which depend on constitutive law and loading path angle can be calculated analytically, based on (2.12) and (2.13). The following three figures give the minimum δ_- and maximum δ_+ influence disc sizes as functions of the load orientation angle ψ for the three different plasticity models considered and for three different power-law hardening exponents, Fig. 15 for $n = 0.1$, Fig. 16 for $n = 0.22$ (typical of Al alloys) and Fig. 17 for $n = 0.40$ (typical of steel alloys). Curves in the $\psi < 0$ range are terminated when one of the stresses becomes compressive ($\sigma_2 < 0$) (applicable for the calculation of δ_-) or when a finite value of the influence disc cannot be found (applicable for the calculation of δ_+).

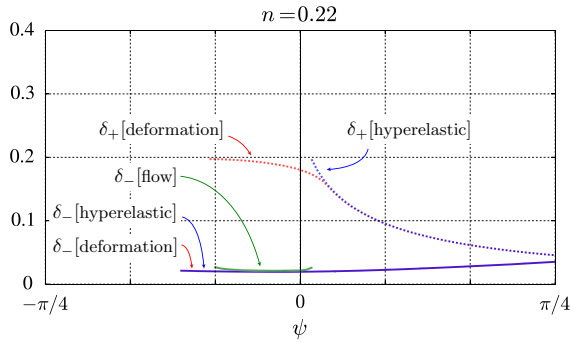

Fig. 16 Minimum δ_- and maximum δ_+ influence disc sizes, in *dashed* and *solid lines* respectively, as functions of the load orientation angle ψ for the three different constitutive models considered, all sharing the same uniaxial *stress-strain curve* with $\epsilon_y = 0.002$, $n = 0.22$

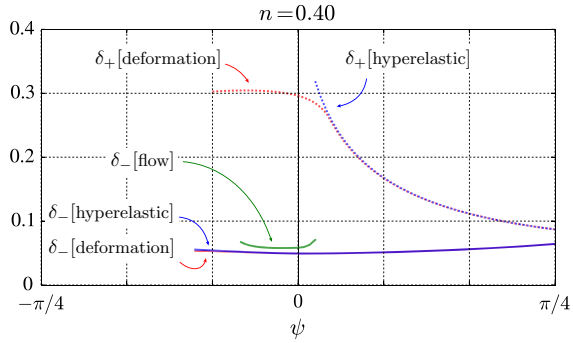

Fig. 17 Minimum δ_- and maximum δ_+ influence disc sizes, in *dashed* and *solid lines* respectively, as functions of the load orientation angle ψ for the three different constitutive models considered, all sharing the same uniaxial *stress-strain curve* with $\epsilon_y = 0.002$, $n = 0.40$

As expected, for a given material and load orientation ψ, both δ_- and δ_+ are increasing functions of the hardening exponent n. There is practically no difference for the minimum influence disc size δ_- between the J_2 deformation and hyperelastic theory models over the entire range of load orientations of interest. However the maximum influence disc size δ_+ predictions for the same two constitutive models coincide only for a certain range of $\psi > 0$. As the uniaxial strain is approached $\psi = 0$, the stiffer hyperelastic theory predicts no finite maximum influence disc size δ_+, in contrast to the J_2 deformation theory that predicts finite δ_+ for a significant range of $\psi < 0$.

There is however a significant difference in the predictions of the much stiffer J_2 flow theory that considerably overestimates δ_- over the other two constitutive models (the difference increasing with increasing hardening exponent n) for the range that a reasonable loss of ellipticity strain can be found (essentially in the range $\psi \leq 0$) and which does not have a δ_- for strain paths with $\psi \leq 0$, given that the J_2 flow theory model does not predict loss of ellipticity for these loadings. Also notice that the J_2 flow theory has no finite δ_+ for any loading.

The difference in the minimum δ_- and maximum δ_+ influence disc sizes predicted by the different constitutive models (in particular between deformation and flow theories) is indicative of the difficulty in predicting failure patterns in these structures and their extreme sensitivity to the constitutive model chosen.

4 Conclusion

This work pertains to the influence of loading rate on the stability of structures when inertia plays a dominant role. The currently established approach to study these stability problems is the method of modal analysis, which determines the structure's fastest growing eigenmode. This method supposes that all points in the structure can be perturbed simultaneously, an assumption that is not appropriate for cases when the velocity of material points in the structure are comparable to the associated wave propagation speeds.

The novel idea here is to analyze the evolution of spatially localized perturbations of the time-dependent, high-strain-rates states of these structures, in order to understand the initiation of the corresponding failure mechanisms. Following the recent analysis by Ravi-Chandar and Triantafyllidis (2015) in 1D bars, we study the high strain extension of a 2D, incompressible, elastoplastic (rate-independent) plate. Using a nonlinear constitutive law makes sense for real structures since no unloading occurs until a point in the structure reaches the loss of ellipticity condition, at which point our calculations are terminated.

Using a finite strain deformation theory of plasticity (based on logarithmic strain), we follow the time evolution of spatially localized perturbations and their interactions. The nonlinear time evolution of such a perturbation is studied numerically using FEM and it is shown that these structures are stable until the time when the condition for the loss of ellipticity is reached. An analytical method, based on linearization, is used to define the size of the influence zone of a point-wise per-

turbation and we study its dependence on constitutive laws and loading conditions.

The above approach is useful for the stability analysis of more realistic structures under high strain rates. As one such example we cite the recent work by Putelat and Triantafyllidis (2014) on the stability of a pressurized thin ring at high rates, where it is shown that for small values of the applied loading rate, the structure fails through a global mode, while for large values of the applied loading rate the structure fails by a localized mode of deformation, as also found recently in the experiments of Mainy and Ravi-Chandar (2014). Our study also shows the sensitivity of the size of minimum and maximum influence zones with respect to the constitutive model used, and hence the caution needed in using such calculations to predict failure patterns.

Acknowledgments The authors would like to thank Prof. K. Ravi-Chandar from the Aerospace Engineering and Engineering Mechanics Department of the University of Texas at Austin for many helpful discussions during the course of this work. Financial support for this project from the Ecole Polytechnique and the Commissariat à l Energie Atomique et aux Energies Alternatives (CEA) is gratefully acknowledged.

References

Abeyaratne R, Triantafyllidis N (1981) The emergence of shear bands in plane strain. Int J Solids Struct 17(1113–1134):00043

Brush D, Almroth B (1975) Buckling of bars, plates, and shells. McGraw-Hill I, New York

Budiansky B, Hutchinson J (1964) Dynamic buckling of imperfection sensitive structures. In: Proceedings XI international congress of applied mechanics, Munich

Guduru P, Freund L (2002) The dynamics of multiple neck formation and fragmentation in high rate extension of ductile materials. Int J Solids Struct 39:5615–5632

Hilber HM, Hughes TJR, Taylor RL (1977) Improved numerical dissipation for time integration algorithms in structural dynamics. Earthq Eng Struct Dyn 5(283–292):01372

Jouve D (2015) Analytic study of the onset of plastic necking instabilities during biaxial tension tests on metallic plates. Eur J Mech A Solids 50:59–69

Koning C, Taub J (1933) Impact buckling of thin bars in the elastic range hinged at both ends. Luftfahrtfosrchung 10:55–64

Mainy A, Ravi-Chandar K (2014) Dynamic buckling of thin metallic rings under external pressure. Master Thesis, University of Texas, Austin. http://hdl.handle.net/2152/ETD-UT-2012-05-5865

Mercier S, Granier N, Molinari A, Liorca F, Buy F (2010) Multiple necking duringt hedynamic expansion of hemisph erical metallic shells, from experiments to modelling. J Mech Phys Solids 58:955–982

Mercier S, Molinari A (2003) Predictions of bifurcation and instabilities during dynamic extension. Int J Solids Struct 40:1995–2016

Putelat T, Triantafyllidis N (2014) Dynamic stability of externally pressurized elastic rings subjected to high rates of loading. Int J Solids Struct 51:1–12

Ravi-Chandar K, Triantafyllidis N (2015) Dynamic stability of a bar under high loading rate: response to local perturbations. Int J Solids Struct 58:301–308

Shenoy V, Freund L (1999) Necking bifurcations during high strain rate extension. J Mech Phys Solids 47:2209–2233

Sorensen N, Freund L (2000) Unstable neck formation in a ductile ring subjected to impulsive radial loading. Int J Solids Struct 37:2265–2283

Stören S, Rice JR (1975) Localized necking in thin sheets. J Mech Phys Solids 23:421–441

Xue Z, Vaziri A, Hutchinson J (2008) Material aspects of dynamic neck retardation. J Mech Phys Solids 56:93–113

Zhang H, Ravi-Chandar K (2006) On the dynamics of necking and fragmentation-I. real-time and post-mortem observations in al 6061-O. Int J Fract 142:183–217

Zhang H, Ravi-Chandar K (2008) On the dynamics of necking and fragmentation-II. effect of material properties, geometrical constraints and absolute size. Int J Fract 150:3–36

Zhang H, Ravi-Chandar K (2010) On the dynamics of necking and fragmentation-iv. expansion of al 6061-o tubes. Int J Fract 163:41–65

Zhou F, Molinari J, Ramesh KT (2006) An elastic-visco-plastic analysis of ductile expanding ring. Int J Impact Eng 33:880–891